

Article

Assessing the Interfacial Dynamic Modulus of Biological Composites

Yaniv Shelef ^{1,†} , Avihai Yosef Uzan ^{1,†}, Ofer Braunshtein ^{1,2} and Benny Bar-On ^{1,*} 

¹ Department of Mechanical Engineering, Ben-Gurion University of the Negev, Beer Sheva 84105, Israel; shelefy@post.bgu.ac.il (Y.S.); uzanav@post.bgu.ac.il (A.Y.U.); ofbr@post.bgu.ac.il (O.B.)

² Nuclear Research Center-Negev, P.O. Box 9001, Beer-Sheva 84190, Israel

* Correspondence: bbo@bgu.ac.il

† Authors with equal contributions.

Abstract: Biological composites (biocomposites) possess ultra-thin, irregular-shaped, energy dissipating interfacial regions that grant them crucial mechanical capabilities. Identifying the dynamic (viscoelastic) modulus of these interfacial regions is considered to be the key toward understanding the underlying structure–function relationships in various load-bearing biological materials including mollusk shells, arthropod cuticles, and plant parts. However, due to the submicron dimensions and the confined locations of these interfacial regions within the biocomposite, assessing their mechanical characteristics directly with experiments is nearly impossible. Here, we employ composite-mechanics modeling, analytical formulations, and numerical simulations to establish a theoretical framework that links the interfacial dynamic modulus of a biocomposite to the extrinsic characteristics of a larger-scale biocomposite segment. Accordingly, we introduce a methodology that enables back-calculating (via simple linear scaling) of the interfacial dynamic modulus of biocomposites from their far-field dynamic mechanical analysis. We demonstrate its usage on zigzag-shaped interfaces that are abundant in biocomposites. Our theoretical framework and methodological approach are applicable to the vast range of biocomposites in natural materials; its essence can be directly employed or generally adapted into analogous composite systems, such as architected nanocomposites, biomedical composites, and bioinspired materials.

Keywords: biological composites; interfaces; dynamic modulus; analytical modeling; composite mechanics



Citation: Shelef, Y.; Uzan, A.Y.; Braunshtein, O.; Bar-On, B. Assessing the Interfacial Dynamic Modulus of Biological Composites. *Materials* **2021**, *14*, 3428. <https://doi.org/10.3390/ma14123428>

Academic Editor: Milena Ignatova

Received: 11 May 2021
Accepted: 16 June 2021
Published: 21 June 2021

Publisher's Note: MDPI stays neutral with regard to jurisdictional claims in published maps and institutional affiliations.



Copyright: © 2021 by the authors. Licensee MDPI, Basel, Switzerland. This article is an open access article distributed under the terms and conditions of the Creative Commons Attribution (CC BY) license (<https://creativecommons.org/licenses/by/4.0/>).

1. Introduction

Load-bearing biocomposites are typically structured as arrays of rigid and predominantly elastic reinforcing elements (e.g., biominerals or crystalline biopolymers), which are connected by a more compliant and energy-dissipating matrix material (e.g., proteins or hemicellulose) through submicron length, compositionally graded, and irregularly-shaped interfacial regions [1–8]. The effective dynamic (viscoelastic) modulus of these interfacial regions provides the biocomposites' diverse mechanical functions, including adsorbing impacts, detaining cracks, and filtering mechanical signals [9–17]. Identifying the interfacial dynamic modulus of biocomposites is a long-standing objective of biomaterial science research [18], it is considered the keystone toward understanding the fundamental structure–function relationships in various biocomposite systems [19–25].

Nanomechanical testing methods, e.g., nanoindentation and nanoscale dynamic mechanical analysis (DMA), are the benchmark approaches to identifying the mechanical characteristics of the interfacial regions in biocomposites [18,26–32]. These methods apply local contact loadings to certain locations within the interfacial region, analyze their mechanical response upon static or harmonic forces, and determine the elastic stiffness and viscous damping characteristics of the underlying reinforcement or matrix materials within the interfacial region. These underlying material characteristics link to the mechanical response of the interfacial region as a whole via shear-lag mechanisms, which transfer

axial loads between adjacent reinforcements through the tensile-shear loadings of their intermediate matrix material [33–36]. Recent studies on planar interfacial morphologies (e.g., staggered, triangular, and trapezoid) have derived analytical relationships between the overall dynamic modulus of the interfacial region and those of its underlying reinforcement and matrix materials [37–41]. However, these analytical relationships cannot account for non-planar, irregularly-shaped, or unmarked interfacial morphologies (as commonly present in natural materials), which must be characterized through direct interfacial experiments. Practically, such direct interfacial experiments are nearly impossible due to the small dimensions and the confined locations of the interfacial regions within the biocomposite complex. The interfacial mechanical characteristics must be analytically extracted from far-field experiments on a larger-scale biocomposite segment [42–46]. Even small variations in the interfacial characteristics, i.e., material properties or relative content within the biocomposite, may substantially affect the mechanical response of the biocomposite segment [47–49]. Establishing feasible methodologies to approach the interfacial dynamic modulus of biocomposites from far-field experiments is a pending challenge of both biological and synthetic nanomaterial science [50–54].

Here, we employ composite-mechanics modeling, theoretical approximations, and numerical simulations to identify simple analytical relationships between the dynamic modulus (i.e., modulus magnitude and loss coefficient) of an interfacial region within a biocomposite to its larger-scale, enclosing biocomposite segment. With these relationships, we propose an analytical methodology that allows for the back-calculation (linear scaling) of the interfacial dynamic modulus from far-field DMA results on the biocomposite segment. Finally, we demonstrate the usability and adequacy of our methodology via numerical experiments on a class of sutural interfaces that are abundant in natural materials.

2. Analytical Relationships for the Interface–Biocomposite Dynamic Moduli

We considered a biocomposite segment—an isolated specimen from a larger-scale biocomposite complex—that includes adjacent elastic reinforcements connected by an energy-dissipating, viscoelastic matrix in various possible structural forms (Figure 1a). We identified the interfacial region (of length L_i) within the biocomposite segment (of length L_c) as the region that is different from the pristine reinforcements in terms of material properties or architectural characteristics. We characterized the elastic behavior of the reinforcements via Young’s modulus E_f and the viscoelastic behavior of the whole biocomposite segment via the dynamic (complex) modulus $E_c^* = E_c \cdot e^{j \cdot \delta_c}$, where E_c is the modulus magnitude of the biocomposite, and $\tan \delta_c$ is the loss coefficient of the biocomposite. We characterized the viscoelastic behavior of the interfacial region by an effective dynamic modulus $E_i^* = E_i \cdot e^{j \cdot \delta_i}$ that compiles the properties of its underlying reinforcement and matrix materials via the interfacial shear-lag mechanisms (E_i and $\tan \delta_i$ are the effective modulus magnitude and the effective loss coefficient of the interfacial region, respectively).

To connect the interfacial dynamic modulus (E_i^*) to that of the whole biocomposite segment (E_c^*), we modeled the biocomposite segment as a reinforcement-interface-reinforcement sequence (Figure 1b) and employed Reuss’s model from classical composite mechanics (adapted via the correspondence principle) [49,55], which aptly describes various analogous biocomposite configurations, both at the macromolecular level (e.g., nanofibrils) [44], the nanocomposite level (e.g., nanofibril arrays enriched with biominerals) [3], and the microcomposite level (e.g., lamellar architectures) [56]. Consequentially, we expressed E_i^* as follows [49,55]:

$$E_i^* = \left[\frac{1/(L_i/L_c)}{E_c^*} - \frac{1/(L_i/L_c) - 1}{E_f} \right]^{-1} \quad (1)$$

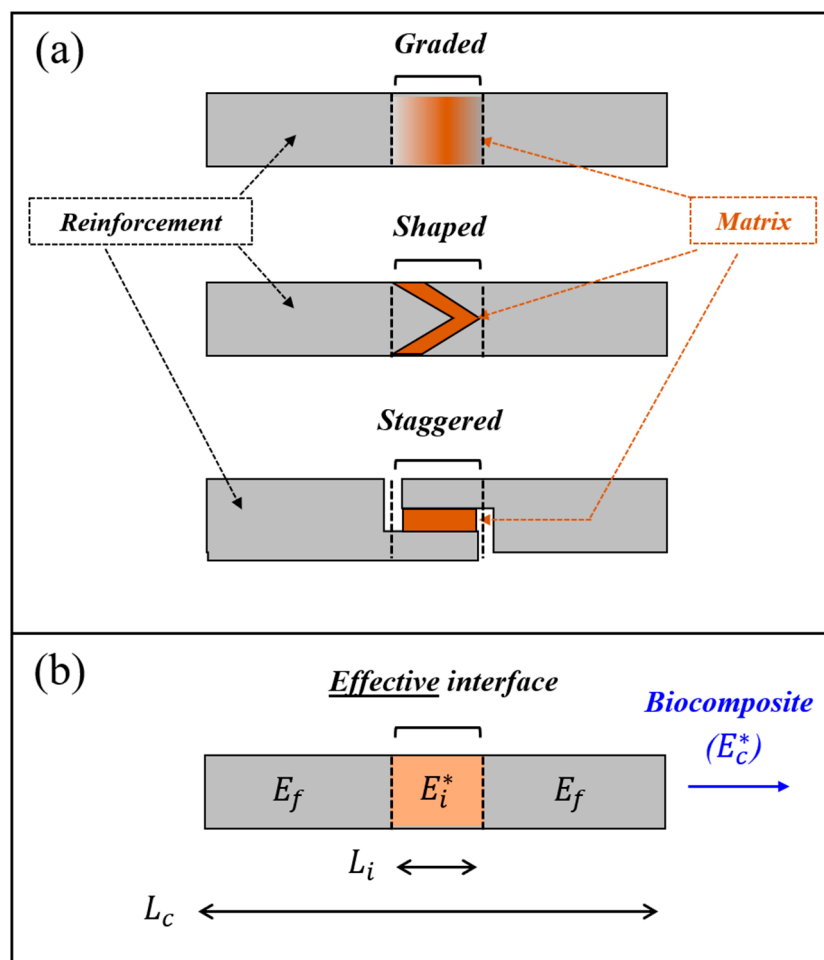


Figure 1. (a) Schematic examples of the interfacial regions in biocomposites: graded matrix properties, shaped matrix-reinforcement connection, and staggered matrix-reinforcement connection. (b) Mechanical modeling of a biocomposite segment (length L_c and dynamic modulus E_c^*), which includes an effective viscoelastic interface (length L_i and dynamic modulus E_i^*) between adjacent elastic reinforcements (elastic modulus E_f).

Practically, the biocomposite dynamic modulus (E_c^*) is characterized by small-scale DMA experiments, e.g., atomic force microscopy or dynamic nanoindentation, which yield E_c and $\tan \delta_c$ from the amplitude ratio and the phase shift between the harmonic stress and strain signals, respectively. Thus, we wished to draw direct analytical connections between these experimental measures (E_c and $\tan \delta_c$) to the corresponding characteristics of the interfacial region (E_i and $\tan \delta_i$). By employing standard analytical steps (see Section S1 in Supporting Information) into Equation (1), we obtained the following equivalent equations:

$$E_i = E_c \cdot \frac{L_i}{L_c} \cdot \frac{1}{\sqrt{1 - 2 \cdot \left(1 - \frac{L_i}{L_c}\right) \cdot \left(\frac{E_c}{E_f}\right) \cdot \frac{1}{\sqrt{1 + \tan^2 \delta_c}} + \left(\frac{E_c}{E_f}\right)^2 \cdot \left(1 - \frac{L_i}{L_c}\right)^2}} \quad (2)$$

$$\tan \delta_i = \tan \delta_c \cdot \frac{1}{1 - \frac{E_c}{E_f} \cdot \left(1 - \frac{L_i}{L_c}\right) \cdot \sqrt{1 + \tan^2 \delta_c}} \quad (3)$$

Next, we considered the typical mechanical characteristics of biocomposites, $E_c/E_f \leq 1/4$ and $\tan \delta_c \leq 1/2$ (which are mostly far below these bounds; see [18] and the

references therein), introduced analytical approximations into Equations (2) and (3), and obtained the following relationships (see section S1 in Supporting Information):

$$E_i = k_E \cdot E_c; k_E = \frac{L_i/L_c}{1 - (E_c/E_f) \cdot (1 - L_i/L_c)} \quad (4)$$

$$\tan \delta_i = k_\delta \cdot \tan \delta_c; k_\delta = \frac{1}{1 - (E_c/E_f) \cdot (1 - L_i/L_c)} \quad (5)$$

Equations (4) and (5) show that the interface–biocomposite characteristics, $E_i - E_c$ and $\tan \delta_i - \tan \delta_c$, link via linear scaling. The scaling factors, k_E and k_δ , depend only on the biocomposite-to-reinforcement modulus ratio (E_c/E_f) and the relative length of the interface within the biocomposite (L_i/L_c), and exclude the loss coefficient of the biocomposite ($\tan \delta_c$). Specifically, when the biocomposite-to-reinforcement modulus ratio is sufficiently small ($E_c/E_f < 1/10$), or when the relative length of the interfacial region is sufficiently large ($1/2 < L_i/L_c$), the denominators of k_E and k_δ approaches unity, and Equations (4) and (5) further simplify into $E_i \approx L_i/L_c \cdot E_c$ and $\tan \delta_i \approx \tan \delta_c$. Notably, as k_E and k_δ are nondimensional, the $E_i - E_c$ and $\tan \delta_i - \tan \delta_c$ relationships in Equations (4) and (5) are independent of the absolute length scale and the mechanical characteristics of the biocomposite. Consequentially, these $E_i - E_c$ and $\tan \delta_i - \tan \delta_c$ relationships are generally applicable for the broad dimensional range of biocomposites in natural materials—including macromolecular, nanoscale, and microscale biocomposites—and their diverse mechanical characteristics, i.e., from highly rigid to substantially compliant and from nearly elastic to prominently viscous.

We employed numerical dynamic mechanical analysis via finite element (FE) simulations (Abaqus 6.12, T2D2H elements) to verify the interface–biocomposite relationships in Equations (4) and (5). We analyzed a biocomposite segment (length L_c) that was comprised of a pair of elastic reinforcements (elastic modulus E_f) and an intermediate viscoelastic interface (length L_i and dynamic modulus $E_i^* = E_i \cdot e^{j\delta_m}$). In each simulation, we applied harmonic strain loadings on the lateral edges of the biocomposite segment, probed the resulting harmonic stresses on these edges, and extracted the modulus magnitude and the loss coefficient of the biocomposite (E_c and $\tan \delta_c$) from the amplitude ratio and the phase shift between the stress and strain signals. We analyzed the simulation models with a wide range of input parameters that enclosed the typical characteristics of natural materials (see Tables S1 and S2 in the Supporting Information), we plotted their resultant pairs, $E_i - E_c$ pairs (Figure 2), and $\tan \delta_i - \tan \delta_c$ pairs (Figure 3). For each simulation model, we calculated the biocomposite-to-reinforcement modulus ratio (E_c/E_f), the relative length of the interfacial region within the biocomposite (L_i/L_c), and the resultant interface–biocomposite scaling factors (k_E and k_δ , respectively). Then, we plotted the theoretical relationships in Equations (4) and (5) with the $E_i - E_c$, and $\tan \delta_i - \tan \delta_c$ pair sets from the numerical simulations (Figures 2 and 3) which showed excellent correspondence for the entire range of input parameters analyzed.

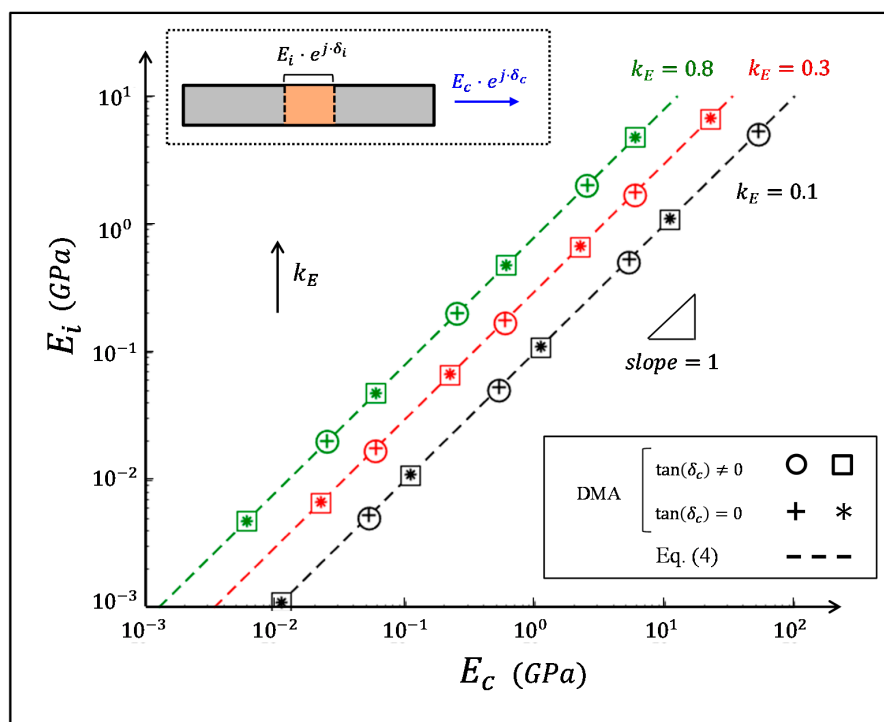


Figure 2. The correspondence between E_i and E_c for various biocomposite configurations. The dashed lines indicate the theoretical results via Equation (4), and the symbols indicate the corresponding finite-element results (Table S1 in Supporting Information). The colors indicate data sets with the same k_E parameter: black, red, and green correspond to $k_E = 0.1$, 0.3 , and 0.8 , respectively. The circle and square symbols represent different viscoelastic biocomposite configurations ($\tan \delta_c \neq 0$), while the plus and asterisk symbols represent the corresponding biocomposite configurations, but with completely elastic properties ($\tan \delta_c = 0$).

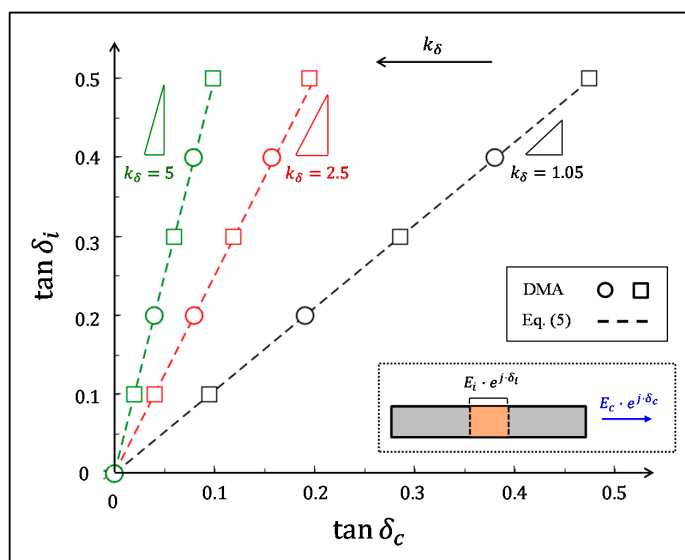


Figure 3. The correspondence between $\tan \delta_i$ and $\tan \delta_c$ for various biocomposite configurations. The dashed lines indicate the theoretical results via Equation (4), and the symbols indicate the corresponding finite-element results (Table S2 in Supporting Information). The colors indicate data sets with the same k_δ parameter: black, red, and green correspond to $k_\delta = 1.05$, 2.5 , and 5 , respectively. The range of $\tan \delta_i$ spans between completely elastic ($\tan \delta_i = 0$) and predominantly viscoelastic ($\tan \delta_i = 1/2$) interfaces.

3. Assessing the Interfacial Dynamic Modulus from a Far-Field Dynamic Mechanical Analysis

3.1. Methodological Approach

We have used the interface–biocomposite relationships in Equations (4) and (5) to propose the following methodological approach to back-calculate the interfacial dynamic modulus from far-field DMA measurements on the biocomposite segment itself.

Step 1: Isolate a testing segment (length L_c) from the biocomposite complex and use microscopy observations to identify its underlying interfacial region (length L_i).

Step 2: Apply DMA testing on a biocomposite segment and quantify its modulus magnitude and loss coefficient (E_c and $\tan \delta_c$).

Step 3: Use nanomechanical testing (or the literature data) to determine the elastic modulus of the reinforcements (E_f) outside the interfacial region.

Step 4: Calculate the interface–biocomposite scaling factors (k_E and k_δ), and use them to back-calculate the modulus magnitude and the loss coefficient of the interfacial region from the corresponding biocomposite characteristics ($E_i = k_E \cdot E_c$, and $\tan \delta_i = k_\delta \cdot \tan \delta_c$).

Practically, the estimations of L_i and E_f (Steps 1 and 3 above) typically incorporate certain deviation ranges, which arise from the resolution limitation of the microscopy analysis, and from the inherent variability of the nanomechanical analysis, respectively, such that $L_i \rightarrow L_i \pm \Delta L_i$, and $E_f \rightarrow E_f \pm \Delta E_f$. Accordingly, the interface–biocomposite scaling factors also include deviation ranges $k_E \rightarrow k_E \pm \Delta k_E$, and $k_\delta \rightarrow k_\delta \pm \Delta k_\delta$. To identify these deviations, we calculated the first-order differentials of Equations (4) and (5), namely $\Delta k_E = dk_E/dL_i \cdot \Delta L_i + dk_E/dE_f \cdot \Delta E_f$, and $\Delta k_\delta = dk_\delta/dL_i \cdot \Delta L_i + dk_\delta/dE_f \cdot \Delta E_f$, and we expressed them analytically as follows:

$$\Delta k_E = k_E \cdot \left[(1 - A) \cdot \frac{\Delta L_i}{L_i} - B \cdot \frac{\Delta E_f}{E_f} \right] \quad (6)$$

$$\Delta k_\delta = k_\delta \cdot \left[-A \cdot \frac{\Delta L_i}{L_i} - B \cdot \frac{\Delta E_f}{E_f} \right] \quad (7)$$

where

$$A = \frac{L_i}{L_c} \cdot \frac{E_c}{E_f} \cdot \frac{1}{C}, \quad B = \frac{E_c}{E_f} \cdot \left[1 - \frac{L_i}{L_c} \right] \cdot \frac{1}{C}, \quad C = 1 - \left(\frac{E_c}{E_f} \right) \cdot \left(1 - \frac{L_i}{L_c} \right) \quad (8)$$

Notably, when the interfacial region occupies large portions of the biocomposite segment ($L_i/L_c \rightarrow 1$), the coefficients $B \ll A$, and the k_E and k_δ deviations reduce into $\Delta k_E \approx k_E \cdot (1 - A) \cdot \Delta L_i/L_i$ and $\Delta k_\delta \approx -k_\delta \cdot A \cdot \Delta L_i/L_i$; both k_E and k_δ are insensitive to E_f deviations. Moreover, when the biocomposite-to-reinforcement modulus ratio is sufficiently small ($E_c/E_f < 1/10$), the coefficients $A, B \ll 1$, and the k_E and k_δ deviations, further simplify into $\Delta k_E \approx k_E \cdot \Delta L_i/L_i$ and $\Delta k_\delta \ll k_\delta$; the k_E deviations are proportional to the L_i deviations, and the k_δ deviations are approximately negligible.

Next, we demonstrate our approach on biocomposites with zigzag-shaped sutural interfaces and illustrate the effect of their zigzag angles on the modulus magnitude and the loss coefficient of these interfacial regions.

3.2. Example: Sutural Interfaces

Sutural interfaces are abundant in natural materials, such as dermal armors [57,58], bird beaks [59], and seed coats [60], and they serve as locally flexible and energy-dissipating regions within a much harder and fragile bulk material. These sutural interfaces commonly view periodic zigzag geometries (period length λ_i , zigzag angle θ), which connect adjacent elastic reinforcements (elastic modulus E_f) via a viscoelastic matrix layer (length L_m , dynamic modulus $E_m^* = E_m \cdot e^{j \cdot \delta_m}$), and yield an interfacial region of length $L_i = L_m + \lambda_i/2 \cdot \tan \theta$ (Figure 4). The zigzag angle of these sutural interfaces plays a major

role in the various mechanical functions of the sutural interfaces, e.g., its elastic stiffness, failure strength, damping capability, and impact resistance [11,36,61,62]. Here, we use numerical simulations to demonstrate the effect of the zigzag angle of the sutural interface on its effective dynamic modulus [41]. We focus on sutural interfaces with substantial matrix portions ($L_m/\lambda_i = 1/4$) and small-to-moderate zigzag angles ($\theta = 0 \rightarrow 75^\circ$), which complement the framework of corresponding analytical models and extract the effective modulus magnitude and loss coefficient of these interfacial regions from a far-field DMA analysis of a biocomposite segment via the above methodological approach (Section 3.1). We used plane stress FE simulations (Abaqus 6.12, CPS4 elements) with a substantially viscoelastic matrix (loss coefficient $\tan \delta_m = 1/2$), and much stiffer, elastic reinforcements ($E_f/E_m = 10$). For simplicity, we considered the matrix and reinforcements to be nearly incompressible ($E_f/G_f = E_m^*/G_m^* = 2.5$). For each zigzag angle analyzed (θ), we realized the geometry of the sutural interface ($L_m/\lambda_i = 1/4$, and $L_i/L_m = 1 + 2 \cdot \tan \theta$), and set the remaining length of the reinforcements to ensure that the overall interface-to-composite length ratio was kept constant ($L_i/L_c = 0.1$). For each case, we applied harmonic strain loadings on the lateral edges of the biocomposite (upper and lower edges were free), measured the resulting harmonic stresses on these edges, and extracted the modulus magnitude and the loss coefficient of the biocomposite ($E_c(\theta)/E_m$ and $\tan \delta_c(\theta)$) from the amplitude ratio and the phase shift between the stress and strain signals. Then, we calculated the scaling factors k_E and k_δ factors, and back-calculated the modulus magnitude and the loss coefficient of the sutural interface, $E_i(\theta)/E_m$ and $\tan \delta_i(\theta)$, via Equations (4) and (5), respectively (Figure 5a,b, Table S3 in Supporting Information). To verify our results, we performed a complementary analysis on the isolated sutural interfaces (i.e., $L_i/L_c = 1$) that directly yielded $E_i(\theta)/E_m$ and $\tan \delta_i(\theta)$ (i.e., without back-calculations); evidently, our estimations from the far-field DMA analysis on the biocomposite segments are in good agreement with the direct analysis on the isolated sutural interfaces for the entire θ range analyzed. Our results show that the zigzag angle strongly affects the modulus magnitude and the loss coefficient of the sutural interface (Figure 5a,b), and are in line with the theoretical trends of recent analytical studies [41]. As the zigzag angle approaches zero, the interfacial region is almost flat and mostly comprises the matrix layer ($L_i/L_m \sim 1$), and its modulus magnitude and loss coefficient approach that of the pristine matrix material $E_i(\theta \rightarrow 0) \sim E_m$ and $\tan \delta_i(\theta \rightarrow 0) \sim \tan \delta_m$. Conversely, as the zigzag angle increases, the interfacial region occupies greater portions of the stiffer elastic reinforcements (in addition to the matrix layer), which results in a progressive increase in the modulus magnitude of the interfacial region $E_i(\theta)$ and a complementary decrease in its loss coefficient $\tan \delta_i(\theta)$. Thus, natural sutural interfaces with similar matrix and reinforcement characteristics can achieve different biomechanical functions merely through morphological adaptations of their zigzag shapes. Mild zigzag shapes will generate interfacial regions with greater flexibility and higher energy-dissipation capabilities, whereas acute zigzag shapes will generate interfacial regions with greater robustness and higher energy-storing capabilities.

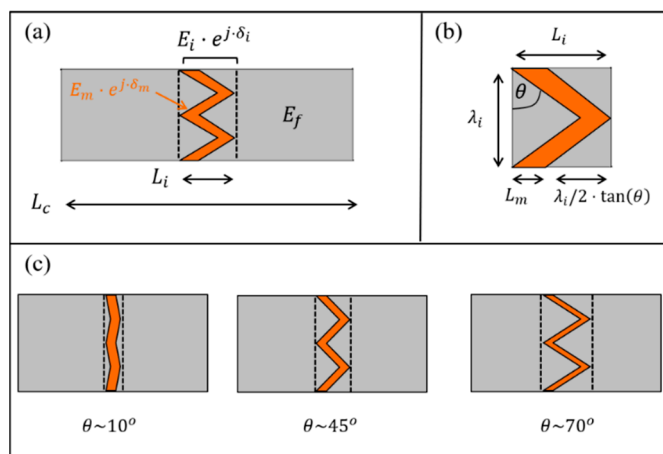


Figure 4. Schematic descriptions of zigzag-shaped sutural interfaces in biocomposites and their geometrical parameters. (a) A biocomposite segment with an underlying sutural interface. (b) An isolated interfacial region (one period) from the biocomposite. (c) Schematic examples of sutural interfaces with the same matrix length (L_m), but different zigzag angles ($\theta = 10^\circ, 45^\circ$, and $\sim 70^\circ$).

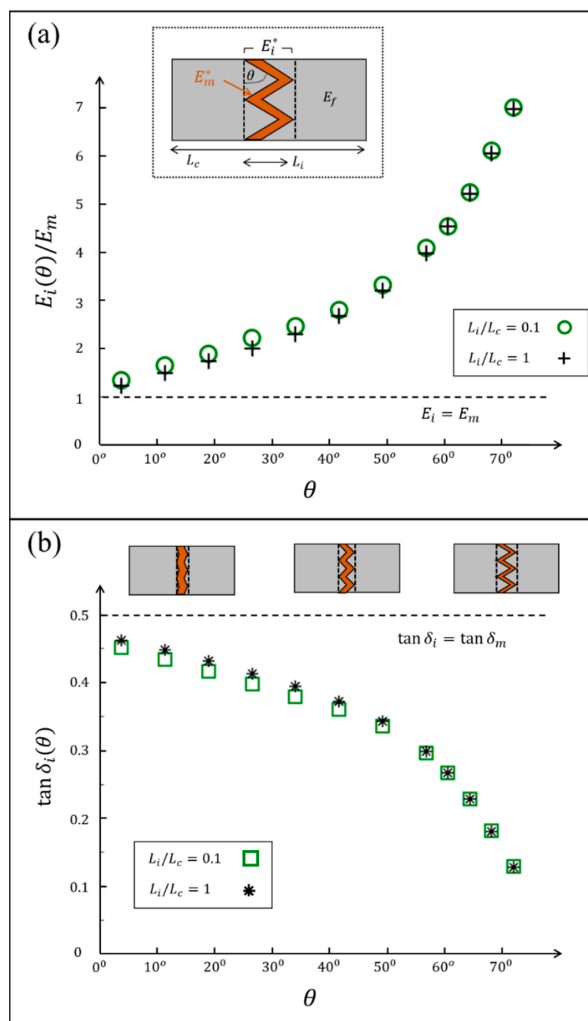


Figure 5. Simulation results for the interfacial dynamic modulus of biocomposites with zigzag-shaped sutural interfaces. (a) the modulus magnitude and (b) the loss coefficient of the interfacial region for different zigzag angles (θ), achieved by back-calculations from far-field DMA testing on the biocomposite ($L_i/L_c = 0.1$), and by direct DMA testing on the interfacial region ($L_i/L_c = 1$).

4. Conclusions

The interfacial dynamic modulus of biocomposites dominates the structure–function relationships in various organisms, including vertebrates (e.g., mammals, birds, and fishes), invertebrates (e.g., insects, arachnids, and mollusks), and plants. Nevertheless, due to the small dimensions and the confined locations of these interfacial regions, measuring their direct mechanical characterizations is nearly impossible. In this study, we established compact analytical formulae that link the modulus magnitude and the loss coefficient of the interfacial region to those of its enclosing, large-scale, biocomposite segment. We used these formulae to propose an analytical and experimental methodology that yielded the interfacial characteristics via back-calculations, from a feasible, far-field DMA analysis of the biocomposite itself and demonstrated it on zigzag-shaped sutural interfaces. From a broader perspective, our approach can also be used to analyze the interfacial characteristics of advanced engineering materials, such as bioinspired composites, nanocomposites, and electromechanical devices [63–66].

Supplementary Materials: The following are available online at <https://www.mdpi.com/article/10.3390/ma14123428/s1>, Table S1: Summary of DMA simulations results, shown in Figure 2 in the main text; Table S2: Summary of DMA simulations results, shown in Figure 3 in the main text; Table S3: Summary of the DMA simulation results for the zigzag-shaped interfaces and the corresponding back-calculations of E_i and $\tan \delta_i$ via Equations (4) and (5).

Author Contributions: Y.S., A.Y.U. and B.B.-O. conducted the analytical formulations, Y.S., A.Y.U. and O.B. performed the numerical simulations. All authors analyzed and discussed the results and wrote the manuscript. Y.S. and A.Y.U. provided equal contributions. All authors have read and agreed to the published version of the manuscript.

Funding: This research was supported by the Israel Science Foundation (ISF) grant No. 1429/16 and by the German research foundation (DFG) grant GZ: PO 1725/7-1; AOBJ: 639691. The authors acknowledge the generous support of the Pearlstone Center for Aeronautical Engineering Studies.

Institutional Review Board Statement: Not applicable.

Informed Consent Statement: Not applicable.

Data Availability Statement: Data is contained within the article or supplementary material.

Acknowledgments: The authors acknowledge the generous support of the Pearlstone Center for Aeronautical Engineering Studies.

Conflicts of Interest: The authors declare no conflict of interest. The funders had no role in the design of the study; in the collection, analyses, or interpretation of data; in the writing of the manuscript, or in the decision to publish the results.

References

1. Meyers, M.A.; Chen, P.Y.; Lin, A.Y.M.; Seki, Y. Biological materials: Structure and mechanical properties. *Prog. Mater. Sci.* **2008**, *53*, 1–206. [[CrossRef](#)]
2. Dunlop, J.W.; Weinkamer, R.; Fratzl, P. Artful interfaces within biological materials. *Mater. Today* **2011**, *14*, 70–78. [[CrossRef](#)]
3. Bar-On, B.; Wagner, H.D. Structural motifs and elastic properties of hierarchical biological tissues—A review. *J. Struct. Biol.* **2013**, *183*, 149–164. [[CrossRef](#)]
4. Barthelat, F.; Yin, Z.; Buehler, M.J. Structure and mechanics of interfaces in biological materials. *Nat. Rev. Mater.* **2016**, *1*, 16007. [[CrossRef](#)]
5. Shelef, Y.; Bar-On, B. Surface protection in bio-shields via a functional soft skin layer: Lessons from the turtle shell. *J. Mech. Behav. Biomed. Mater.* **2017**, *73*, 68–75. [[CrossRef](#)]
6. Serrano, C.V.; Leemreize, H.; Bar-On, B.; Barth, F.G.; Fratzl, P.; Zolotoyabko, E.; Politi, Y. Ordering of protein and water molecules at their interfaces with chitin nano-crystals. *J. Struct. Biol.* **2016**, *193*, 124–131. [[CrossRef](#)] [[PubMed](#)]
7. Bar-On, B. On the form and bio-mechanics of venom-injection elements. *Acta Biomater.* **2019**, *85*, 263–271. [[CrossRef](#)]
8. Ampaw, E.; Owoseni, T.A.; Du, F.; Pinilla, N.; Obayemi, J.; Hu, J.; Nigay, P.-M.; Nzihou, A.; Uzonwanne, V.; Kana, Z.; et al. Compressive deformation and failure of trabecular structures in a turtle shell. *Acta Biomater.* **2019**, *97*, 535–543. [[CrossRef](#)]
9. Ji, B.; Gao, H. Mechanical properties of nanostructure of biological materials. *J. Mech. Phys. Solids* **2004**, *52*, 1963–1990. [[CrossRef](#)]
10. Smith, B.L.; Schäffer, T.E.; Viani, M.; Thompson, J.B.; Frederick, N.A.; Kindt, J.; Belcher, A.; Stucky, G.D.; Morse, D.E.; Hansma, P.K. Molecular mechanistic origin of the toughness of natural adhesives, fibres and composites. *Nature* **1999**, *399*, 761. [[CrossRef](#)]

11. Lee, N.; Williams, L.N.; Mun, S.; Rhee, H.; Prabhu, R.; Bhattarai, K.R.; Horstemeyer, M.F. Stress wave mitigation at suture interfaces. *Biomed. Phys. Eng. Express* **2017**, *3*, 035025. [[CrossRef](#)]
12. Erko, M.; Younes-Metzler, O.; Rack, A.; Zaslansky, P.; Young, S.L.; Milliron, G.; Chyasnachyus, M.; Barth, F.G.; Fratzl, P.; Tsukruk, T.; et al. Micro-and nano-structural details of a spider's filter for substrate vibrations: Relevance for low-frequency signal transmission. *J. R. Soc. Interface* **2015**, *12*, 20141111. [[CrossRef](#)]
13. Launey, M.E.; Buehler, M.J.; Ritchie, R.O. On the mechanistic origins of toughness in bone. *Annu. Rev. Mater. Res.* **2010**, *40*, 25–53. [[CrossRef](#)]
14. Amini, S.; Tadayan, M.; Idapalapati, S.; Miserez, A. The role of quasi-plasticity in the extreme contact damage tolerance of the stomatopod dactyl club. *Nat. Mater.* **2015**, *14*, 943. [[CrossRef](#)]
15. Huang, W.; Shishehbor, M.; Guarín-Zapata, N.; Kirchhofer, N.D.; Li, J.; Cruz, L.; Wang, T.; Bhowmick, S.; Stauffer, D.; Manimunda, P.; et al. A natural impact-resistant bicontinuous composite nanoparticle coating. *Nat. Mater.* **2020**, *19*, 1236–1243. [[CrossRef](#)]
16. Xu, M.; An, B. Dynamic crack propagation in the turtle carapace. *Mech. Mater.* **2020**, *151*, 103614. [[CrossRef](#)]
17. Jearanaisilawong, P.; Jongpairajcosit, N.; Glunrawd, C. Dynamic behaviors and protection mechanisms of sulcata tortoise carapace. *Comput. Methods Biomech. Biomed. Eng.* **2021**, 1–13. [[CrossRef](#)] [[PubMed](#)]
18. Zlotnikov, I.; Zolotoyabko, E.; Fratzl, P. Nano-scale modulus mapping of biological composite materials: Theory and practice. *Prog. Mater. Sci.* **2017**, *87*, 292–320. [[CrossRef](#)]
19. Fratzl, P.; Weinkamer, R. Nature's hierarchical materials. *Prog. Mater. Sci.* **2007**, *52*, 1263–1334. [[CrossRef](#)]
20. Meyers, M.A.; McKittrick, J.; Chen, P.Y. Structural biological materials: Critical mechanics-materials connections. *Science* **2013**, *339*, 773–779. [[CrossRef](#)] [[PubMed](#)]
21. Naleway, S.E.; Taylor, J.R.; Porter, M.M.; Meyers, M.A.; McKittrick, J. Structure and mechanical properties of selected protective systems in marine organisms. *Mater. Sci. Eng. C* **2016**, *59*, 1143–1167. [[CrossRef](#)] [[PubMed](#)]
22. Politi, Y.; Bar-On, B.; Fabritius, H.O. Mechanics of Arthropod Cuticle-Versatility by Structural and Compositional Variation. In *Architected Materials in Nature and Engineering*; Springer: Cham, Switzerland, 2019; pp. 287–327.
23. Shtein, I.; Koyfman, A.; Eshel, A.; Bar-On, B. Autotomy in plants: Organ sacrifice in *Oxalis* leaves. *J. R. Soc. Interface* **2019**, *16*, 20180737. [[CrossRef](#)]
24. Bentov, S.; Palmer, B.A.; Bar-On, B.; Shelef, Y.; Aflalo, E.D.; Sagi, A. Reinforcement of bio-apatite by zinc substitution in the incisor tooth of a prawn. *Acta Biomater.* **2021**, *120*, 116–123. [[CrossRef](#)]
25. Shtein, I.; Bar-On, B.; Popper, Z.A. Plant and algal structure: From cell walls to biomechanical function. *Physiol. Plant* **2018**, *164*, 56–66. [[CrossRef](#)] [[PubMed](#)]
26. Ebenstein, D.M.; Pruitt, L.A. Nanoindentation of biological materials. *Nano Today* **2006**, *1*, 26–33. [[CrossRef](#)]
27. Moshe-Drezner, H.; Shilo, D.; Dorogoy, A.; Zolotoyabko, E. Nanometer-Scale Mapping of Elastic Modules in Biogenic Composites: The Nacre of Mollusk Shells. *Adv. Funct. Mater.* **2010**, *20*, 2723–2728. [[CrossRef](#)]
28. Zhou, X.; Miao, H.; Li, F. Nanoscale structural and functional mapping of nacre by scanning probe microscopy techniques. *Nanoscale* **2013**, *5*, 11885–11893. [[CrossRef](#)]
29. Li, T.; Zeng, K. Nanoscale elasticity mappings of micro-constituents of abalone shell by band excitation-contact resonance force microscopy. *Nanoscale* **2014**, *6*, 2177–2185. [[CrossRef](#)]
30. Zlotnikov, I.; Shilo, D.; Dauphin, Y.; Blumtritt, H.; Werner, P.; Zolotoyabko, E.; Fratzl, P. In situ elastic modulus measurements of ultrathin protein-rich organic layers in biosilica: Towards deeper understanding of superior resistance to fracture of biocomposites. *RSC Adv.* **2013**, *3*, 5798–5802. [[CrossRef](#)]
31. Labonte, D.; Lenz, A.K.; Oyen, M.L. On the relationship between indentation hardness and modulus, and the damage resistance of biological materials. *Acta Biomater.* **2017**, *57*, 373–383. [[CrossRef](#)] [[PubMed](#)]
32. Shelef, Y.; Bar-On, B. Interfacial indentations in biological composites. *J. Mech. Behav. Biomed. Mater.* **2020**, *114*, 104209. [[CrossRef](#)] [[PubMed](#)]
33. Ji, B.; Gao, H. Mechanical principles of biological nanocomposites. *Annu. Rev. Mater. Res.* **2010**, *40*, 77–100. [[CrossRef](#)]
34. Bar-On, B.; Wagner, H.D. Mechanical model for staggered bio-structure. *J. Mech. Phys. Solids* **2011**, *59*, 1685–1701. [[CrossRef](#)]
35. Bar-On, B.; Wagner, H.D. New insights into the Young's modulus of staggered biological composites. *Mater. Sci. Eng. C* **2013**, *33*, 603–607. [[CrossRef](#)] [[PubMed](#)]
36. Li, Y.; Ortiz, C.; Boyce, M.C. A generalized mechanical model for suture interfaces of arbitrary geometry. *J. Mech. Phys. Solids* **2013**, *61*, 1144–1167. [[CrossRef](#)]
37. Zhang, P.; Heyne, M.A.; To, A.C. Biomimetic staggered composites with highly enhanced energy dissipation: Modeling, 3D printing, and testing. *J. Mech. Phys. Solids* **2015**, *83*, 285–300. [[CrossRef](#)]
38. Qwamizadeh, M.; Zhou, K.; Zhang, Y.W. Damping behavior investigation and optimization of the structural layout of load-bearing biological materials. *Int. J. Mech. Sci.* **2017**, *120*, 263–275. [[CrossRef](#)]
39. Wu, J.; Yuan, H.; Li, L.; Fan, K.; Qian, S.; Li, B. Viscoelastic shear lag model to predict the micromechanical behavior of tendon under dynamic tensile loading. *J. Theor. Biol.* **2018**, *437*, 202–213. [[CrossRef](#)]
40. Liu, J.; Zhu, W.; Yu, Z.; Wei, X. Dynamic shear-lag model for understanding the role of matrix in energy dissipation in fiber-reinforced composites. *Acta Biomater.* **2018**, *74*, 270–279. [[CrossRef](#)]
41. Yu, Z.; Liu, J.; Wei, X. Achieving outstanding damping performance through bio-inspired sutural tessellations. *J. Mech. Phys. Solids* **2020**, *142*, 104010. [[CrossRef](#)]

42. Bar-On, B.; Wagner, H.D. Stiffness of the extrafibrillar phase in staggered biological arrays. *Phys. Rev. Lett.* **2012**, *109*, 078102. [[CrossRef](#)] [[PubMed](#)]
43. Prapavesis, A.; Tojaga, V.; Östlund, S.; van Vuure, A.W. Back calculated compressive properties of flax fibers utilizing the Impregnated Fiber Bundle Test (IFBT). *Compos. Part A Appl. Sci. Manuf.* **2020**, *135*, 105930. [[CrossRef](#)]
44. Khodayari, A.; Hirn, U.; Van Vuure, A.W.; Seveno, D. Inverse rule of mixtures at the nanoscale: Prediction of elastic properties of cellulose nanofibrils. *Compos. Part A Appl. Sci. Manuf.* **2020**, *138*, 106046. [[CrossRef](#)]
45. An, B.; Sun, W. A theory of biological composites undergoing plastic deformations. *J. Mech. Behav. Biomed. Mater.* **2019**, *93*, 204–212. [[CrossRef](#)] [[PubMed](#)]
46. Xu, M.; An, B. An analysis of fracture in staggered mineralized collagen fibril arrays. *Int. J. Solids Struct.* **2020**, *193–194*, 535–549. [[CrossRef](#)]
47. Yu, L.; Ma, Y.; Zhou, C.; Xu, H. Damping efficiency of the coating structure. *Int. J. Solids Struct.* **2005**, *42*, 3045–3058. [[CrossRef](#)]
48. Gusev, A.A.; Lurie, S.A. Loss amplification effect in multiphase materials with viscoelastic interfaces. *Macromolecules* **2009**, *42*, 5372–5377. [[CrossRef](#)]
49. Lurie, S.; Minhat, M.; Tuchkova, N.; Soliaev, J. On remarkable loss amplification mechanism in fiber reinforced laminated composite materials. *Appl. Compos. Mater.* **2014**, *21*, 179–196. [[CrossRef](#)]
50. Bar-On, B.; Bayerlein, B.; Blumtritt, H.; Zlotnikov, I. Dynamic response of a single interface in a biocomposite structure. *Phys. Rev. Lett.* **2015**, *115*, 238001. [[CrossRef](#)] [[PubMed](#)]
51. Bayerlein, B.; Bertinetti, L.; Bar-On, B.; Blumtritt, H.; Fratzl, P.; Zlotnikov, I. Inherent Role of Water in Damage Tolerance of the Prismatic Mineral–Organic Biocomposite in the Shell of Pinna Nobilis. *Adv. Funct. Mater.* **2016**, *26*, 3663–3669. [[CrossRef](#)]
52. Funari, M.F.; Greco, F.; Lonetti, P. Dynamic debonding in layered structures: A coupled ALE-cohesive approach. *Frat. Integrata Strutt.* **2017**, *11*, 524–535. [[CrossRef](#)]
53. Cohen, Y.; Ronen, D.; Ya’akobovitz, A. Mechanical behavior of vertically aligned carbon nanotubes under electrostatic tension. *Sens. Actuators A Phys.* **2019**, *292*, 105–111. [[CrossRef](#)]
54. Cohen, Y.; Ya’akobovitz, A. The influence of thermal loads on the physical properties of carbon nanotubes forests. *Microelectron. Eng.* **2021**, *247*, 111575. [[CrossRef](#)]
55. Gibson, R.F. *Principles of Composite Material Mechanics*; CRC Press: Boca Raton, FL, USA, 2016.
56. Seto, J.; Gupta, H.S.; Zaslansky, P.; Wagner, H.D.; Fratzl, P. Tough lessons from bone: Extreme mechanical anisotropy at the mesoscale. *Adv. Funct. Mater.* **2008**, *18*, 1905–1911. [[CrossRef](#)]
57. Krauss, S.; Monsonego-Ornan, E.; Zelzer, E.; Fratzl, P.; Shahar, R. Mechanical function of a complex three-dimensional suture joining the bony elements in the shell of the red-eared slider turtle. *Adv. Mater.* **2009**, *21*, 407–412. [[CrossRef](#)]
58. Yang, W.; Chen, I.H.; Gludovatz, B.; Zimmermann, E.A.; Ritchie, R.O.; Meyers, M.A. Natural flexible dermal armor. *Adv. Mater.* **2013**, *25*, 31–48. [[CrossRef](#)]
59. Lee, N.; Horstemeyer, M.F.; Rhee, H.; Nabors, B.; Liao, J.; Williams, L.N. Hierarchical multiscale structure–property relationships of the red-bellied woodpecker (*Melanerpes carolinus*) beak. *J. R. Soc. Interface* **2014**, *11*, 20140274. [[CrossRef](#)]
60. Gao, C.; Hasseldine, B.P.; Li, L.; Weaver, J.C.; Li, Y. Amplifying strength, toughness, and auxeticity via wavy sutural tessellation in plant seedcoats. *Adv. Mater.* **2018**, *30*, 1800579. [[CrossRef](#)] [[PubMed](#)]
61. Achrai, B.; Bar-On, B.; Wagner, H.D. Biological armors under impact—Effect of keratin coating, and synthetic bio-inspired analogues. *Bioinspirat. Biomim.* **2015**, *10*, 016009. [[CrossRef](#)] [[PubMed](#)]
62. Liu, L.; Jiang, Y.; Boyce, M.; Ortiz, C.; Baur, J.; Song, J.; Li, Y. The effects of morphological irregularity on the mechanical behavior of interdigitated biological sutures under tension. *J. Biomech.* **2017**, *58*, 71–78. [[CrossRef](#)]
63. Yin, Z.; Hannard, F.; Barthelat, F. Impact-resistant nacre-like transparent materials. *Science* **2019**, *364*, 1260–1263. [[CrossRef](#)]
64. Serra, M.; Arenal, R.; Tenne, R. An overview of the recent advances in inorganic nanotubes. *Nanoscale* **2019**, *11*, 8073–8090. [[CrossRef](#)] [[PubMed](#)]
65. Reddy, S.K.; Ya’akobovitz, A. Electromechanical behavior of graphene foams. *Appl. Phys. Lett.* **2019**, *115*, 211902. [[CrossRef](#)]
66. Ben-Shimon, Y.; Ya’akobovitz, A. Flexible and bio-compatible temperature sensors based on carbon nanotube composites. *Measurement* **2021**, *172*, 108889. [[CrossRef](#)]